ACS Energy LETTERS

http://pubs.acs.org/journal/aelccp

LETTER

Quantitative Molecular-Level Understanding of Electrochemical Aluminum-Ion Intercalation into a Crystalline Battery Electrode

Ankur L. Jadhav, Jeffrey H. Xu, and Robert J. Messinger*

Cite This: *ACS Energy Lett.* 2020, 5, 2842−2848

Read Online

ACCESS | Metrics & More | Article Recommendations | Supporting Information

ABSTRACT: Few materials are known to electrochemically intercalate trivalent aluminum cations, a charge storage mechanism central to rechargeable aluminum-ion battery electrodes. Here, using the chevrel phase Mo_6S_8 as a model crystalline electrode material, we couple electrochemical and solid-state ^{27}Al NMR methods to understand quantitatively the aluminum-ion intercalation mechanism up from the molecular level. Unlike divalent Mg^{2+} cations, trivalent Al^{3+} cations intercalate simultaneously, as opposed to sequentially, into two cavities within the chevrel framework during galvanostatic discharge. Minimal Al^{3+} cation trapping occurs upon deintercalation (<7%). The simultaneous ion intercalation mechanism, as well as slow solid-state ion diffusion, can both be understood in terms of the high charge density of Al^{3+} cations. We also reveal that an amorphous surface layer forms upon aluminum-ion desolvation from molecular chloroaluminate anions in the ionic liquid electrolyte. The results yield quantitative molecular-level understanding of aluminum-ion intercalation in a model crystalline electrode material and establish solid-state ^{27}Al NMR as a powerful characterization tool for rechargeable aluminum-ion batteries.

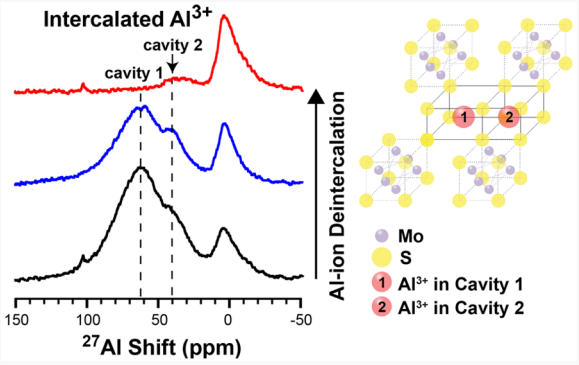

Rechargeable aluminum metal batteries are an emerging energy storage technology with great promise. Aluminum (Al) is the most abundant metal in the earth's crust, low cost, and inherently safe.[1] Aluminum is also energy dense, exhibiting among the highest capacities of common metal electrodes, because of the trivalency of Al^{3+} cations.[2] Despite these opportunities, rechargeable aluminum batteries have been hindered technologically by the small number of positive electrode materials that electrochemically intercalate highly charged Al^{3+} cations.[1,3] In addition, few electrolytes permit reversible electrodeposition of aluminum metal at room temperature.[1] The most common electrolytes are ionic liquids that contain $AlCl_3$ and a salt containing an imidazolium cation with alkyl side chains (e.g., 1-ethyl-3-methylimidazolium chloride, or EMIm) and a halide anion (e.g., Cl^-) in a Lewis acidic mixture (molar ratio of $AlCl_3$:[EMIm]Cl > 1.0), which contain the chloroaluminate anions $AlCl_4^-$ and $Al_2Cl_7^-$.[4−6] Rechargeable aluminum−graphite batteries are technologically promising,[4,7,8] though graphite positive electrodes electrochemically intercalate monovalent $AlCl_4^-$ anions, instead of trivalent Al^{3+} ions, resulting in one- instead of three-electron redox per electroactive ion.

The chevrel Mo_6S_8 is one of the few electrode materials that enables the reversible electrochemical intercalation of several monovalent and multivalent cations (e.g., Li^+, Na^+, Mg^{2+}, Zn^{2+}, etc.),[9−12] including trivalent Al^{3+} cations.[13,14] In particular, the chevrel Mo_6S_8 revolutionized the field of rechargeable magnesium batteries because of its role as a benchmark Mg-ion intercalation electrode.[11,15,16] The chevrel has a unique structure formed by Mo_6S_8 units composed of an Mo_6 octahedron sitting within a chalcogen S_8 cube, which crystallize to form large cavities.[13,17] Two of three cavities permit cation intercalation, where "cavity 1" and "cavity 2" are formed by the corners and edges of Mo_6S_8 units, respectively.[18] Each cavity has six crystallographic sites for small cations that are energetically equivalent.[18] Chevrel phases also exhibit highly

Received: May 24, 2020
Accepted: August 4, 2020
Published: August 4, 2020

https://dx.doi.org/10.1021/acsenergylett.0c01138
ACS Energy Lett. 2020, 5, 2842−2848

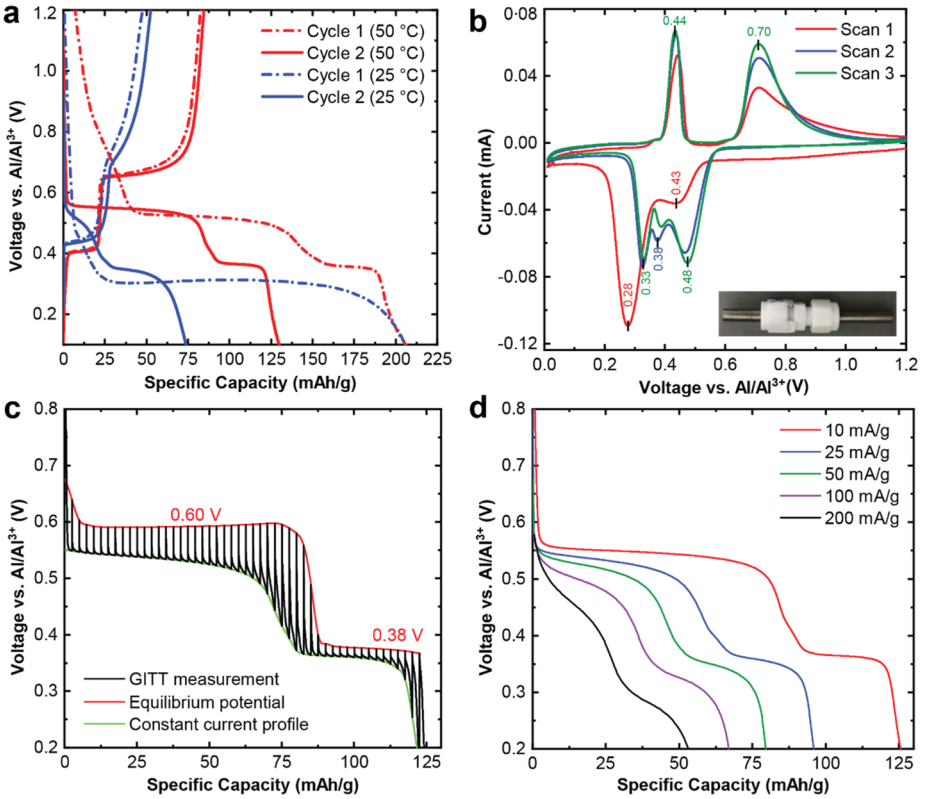

Figure 1. Electrochemical cycling of Al–Mo_6S_8 cells. (a) Galvanostatic cycling (10 mA/g) conducted at 25 °C (blue) and 50 °C (red). (b) Cyclic voltammetry (20 μV/s) performed at 50 °C (inset: PTFE Swagelok cell assembly). (c) GITT measurement (second discharge) performed at 50 °C. (d) Variable-rate galvanostatic discharges (second cycle) performed at 50 °C.

polarizable anionic frameworks, which reduces the energy barrier for cation diffusion.[15,17] Recently, aluminum–chevrel Mo_6S_8 batteries were reported by the groups of Guo[13,19] and Oh,[14] establishing the concept of a rechargeable Al-ion battery electrode.[13] However, quantitative molecular-level understanding of electrochemical Al-ion intercalation into the chevrel Mo_6S_8 has not yet been realized. Understanding the intercalation mechanism, including the effects of the high charge density of trivalent Al^{3+} cations, is vital for designing improved Al-ion intercalation electrodes.

Solid-state nuclear magnetic resonance (NMR) spectroscopy enables battery researchers to selectively probe the intercalated ions themselves, such as identify unique local electronic and magnetic environments associated with intercalation sites, study their dynamics, and quantify their populations.[20−23] Solid-state NMR has been used extensively to study Li-ion intercalation into battery electrodes.[24] However, common multivalent ions such as Mg^{2+}, Ca^{2+}, and Zn^{2+} are challenging to study, as their relevant NMR active nuclei, i.e., ^{25}Mg, ^{43}Ca, and ^{67}Zn, are insensitive because of their low gyromagnetic ratios and natural abundances. Note that despite the vast literature available on Mg-ion intercalation into chevrel Mo_6S_8, to our knowledge, it has not been studied with solid-state ^{25} Mg NMR. In contrast, ^{27}Al nuclei are sensitive because of their high natural abundance (100%) and gyromagnetic ratio (similar to that of ^{13}C). Thus, solid-state ^{27}Al NMR spectroscopy is expected to be a powerful method for investigating Al-ion intercalation into battery electrodes.

Here, we study the reversible electrochemical intercalation of Al^{3+} cations into a battery electrode with solid-state ^{27}Al magic-angle-spinning (MAS) NMR spectroscopy for the first time, using the chevrel Mo_6S_8 as a model crystalline intercalation electrode. We combine quantitative solid-state NMR with electrochemical measurements to better understand the Al-ion intercalation mechanism up from the molecular level. We reveal features unique to the electrochemical intercalation of trivalent Al^{3+} cations, a consequence of their high charge density, and highlight solid-state ^{27}Al NMR spectroscopy as a powerful characterization tool to study rechargeable aluminum-ion batteries.

Galvanostatic cycling, cyclic voltammetry, and galvanostatic intermittent titration technique (GITT) measurements were performed to characterize electrochemically the Al-ion intercalation process. Galvanostatic cycling of Al–Mo_6S_8 cells was conducted at 10 mA/g and either 25 or 50 °C (Figure 1a). Upon first discharge, a sloping voltage profile was observed between the open-circuit potential (1.6 V) and 0.6 V, which is attributed to irreversible electrolyte decomposition that results in additional irreversible capacity.[13,14] After subsequent cycles at 50 °C, two discharge plateaus were observed at 0.55 and 0.38 V, respectively, with an overall capacity of 128 mAh/g. The experimental capacity is in excellent agreement with the theoretical capacity of 128 mAh/g, resulting from the transfer of 4 electrons per Mo_6S_8 unit.[14,25] The discharge capacity during the first discharge plateau is three times that of the second discharge plateau. Thus, the first plateau corresponds to three-electron transfer and intercalation of one Al^{3+} ion per Mo_6S_8 unit, while the second plateau is a result of one-electron transfer and the intercalation of 1/3 of an Al^{3+} ion per Mo_6S_8 unit, resulting in a fully intercalated electrode composition of $Al_{4/3}Mo_6S_8$.[14,19] During charge, the Al^{3+} ions deintercalate from chevrel in the reverse processes. The electrochemical

https://dx.doi.org/10.1021/acsenergylett.0c01138
ACS Energy Lett. 2020, 5, 2842−2848

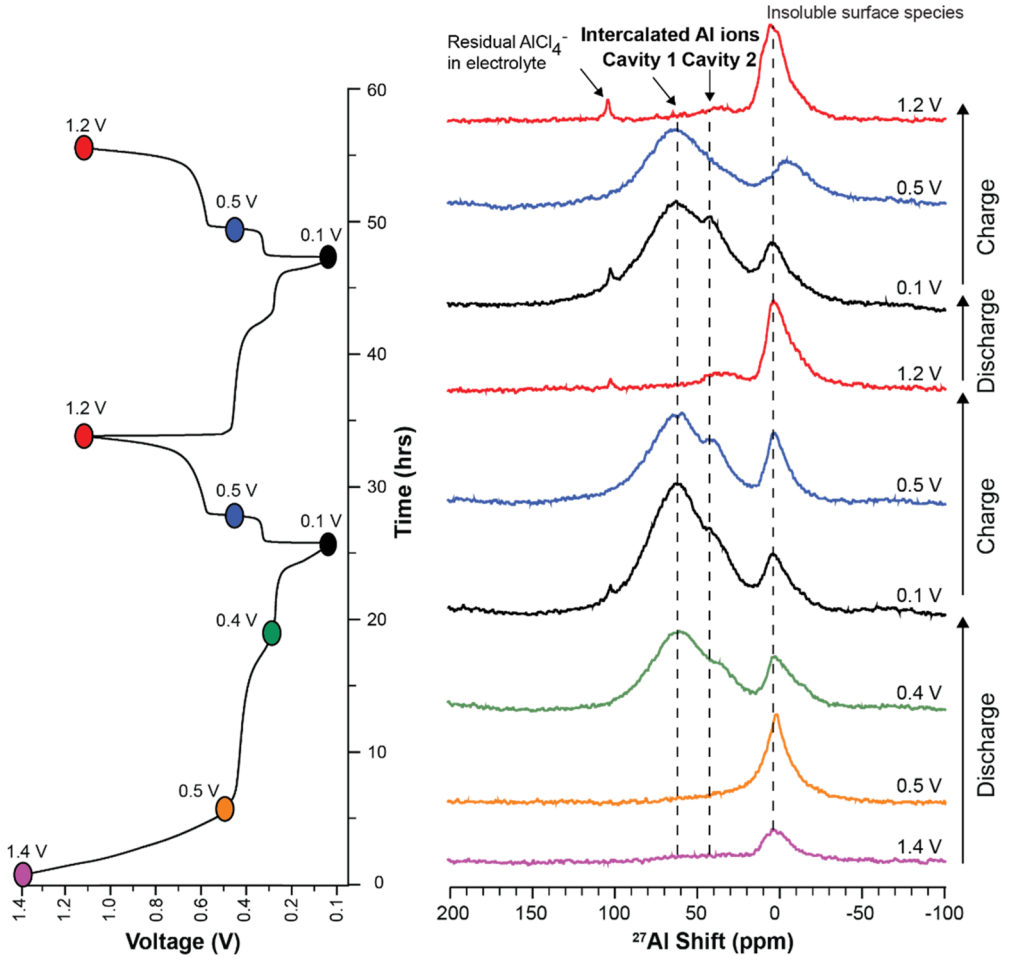

Figure 2. Solid-state ^{27}Al single-pulse MAS NMR spectra (right) of chevrel electrodes from Al−Mo_6S_8 cells galvanostatically cycled to different states-of-charge at 10 mA/g and 50 °C (left), acquired using $\pi/12$ rf pulses under conditions of 20 kHz MAS and 14.1 T. The ^{27}Al signals at 62 and 38 ppm are associated with Al ions intercalated within cavities 1 and 2, respectively. The absolute ^{27}Al signal intensity, scaled by sample mass, increases upon Al-ion intercalation and decreases upon deintercalation.

redox equations associated with the first and second plateaus are shown in eq 1 and 2, respectively:

$$4Al_2Cl_7^- + 3e^- + Mo_6S_8 \rightleftharpoons AlMo_6S_8 + 7AlCl_4^- \quad (1)$$

$$\frac{4}{3}Al_2Cl_7^- + e^- + AlMo_6S_8 \rightleftharpoons Al_{4/3}Mo_6S_8 + \frac{7}{3}AlCl_4^- \quad (2)$$

During charge, the charge capacity is lower than the discharge capacity. We show below that aluminum-ion trapping is minimal (<7%) and hypothesize that self-deintercalation of aluminum ions may explain this difference, a phenomenon possibly linked to the low band gap (1.18 eV, predicted via DFT calculations[26]) between the intercalated ($Al_{4/3}Mo_6S_8$) and deintercalated (Mo_6S_8) chevrel phases.

Galvanostatic cycling at different temperatures reveals the slow solid-state diffusion of highly charged Al^{3+} cations. The discharge capacities are 75 and 128 mAh/g upon the second cycle at 25 and 50 °C, respectively. The specific capacity of the first discharge plateau is approximately three times shorter at 25 °C, while the second discharge plateau exhibits similar capacity. Electrochemical intercalation of Al^{3+} ions is thus diffusion-limited during the first plateau, a result consistent with Al^{3+} diffusion coefficients determined from GITT measurements (see below). Additional galvanostatic cycling and cyclic voltammetry at 25 and 50 °C, including extended galvanostatic cycling, are shown in Figures S1 and S2 (Supporting Information).

Cyclic voltammetry was performed at 20 μV/s and 50 °C (Figure 1b), revealing multiple redox peaks that yield insights into how the strong Coulombic repulsions between Al^{3+} cations affect their electrochemical intercalation. During the first scan, two reduction peaks occur at 0.43 and 0.28 V because of Al^{3+} ion intercalation, followed by two oxidation peaks at 0.44 and 0.70 V that correspond to subsequent Al^{3+} ion deintercalation. Notably, an additional reduction peak at 0.38 V emerges, which persists during subsequent scans. This additional reduction peak is a consequence of strong Coulombic repulsions between intercalated Al^{3+} ions. Because of the higher activation barrier for Al-ion diffusion from cavity 1 (inner ring sites) into cavity 2 (outer ring sites) (0.25 eV, predicted by DFT calculations) compared to that for diffusion among the six energetically equivalent crystallographic sites within cavity 1 (0.08 eV),[26] the Al^{3+} ions preferentially diffuse in circular motions in cavity 1. As intercalation proceeds, the Al^{3+} ions experience increasing extents of cation−cation repulsions that enable them to overcome the potential energy barrier and "hop" from the first to the second cavity, effectively reducing the activation energy barrier for intercalation and resulting in an additional CV reduction peak with reduced

https://dx.doi.org/10.1021/acsenergylett.0c01138
ACS Energy Lett. 2020, 5, 2842−2848

overpotential. Al^{3+} cation "hopping" from cavity 1 to cavity 2 thus occurs before cavity 1 is fully intercalated, consistent with the "simultaneous" Al-ion intercalation mechanism predicted by Geng et al.[19] from Rietveld analyses and as measured below by solid-state ^{27}Al NMR measurements. This phenomenon also results in an inflection point during galvanostatic discharge near 0.38 V for cycle 1 and 0.42 V for cycle 2 (Figure 1a), which can be observed in the corresponding differential capacity (dQ/dV) plots for the first two galvanostatic cycles (Figure S3).

A GITT measurement was performed to measure the equilibrium potentials and to quantify the Al^{3+} ion diffusion coefficients within the crystalline chevrel structure at 50 °C (Figure 1c, second discharge shown).[27,28] The equilibrium potentials of the first and second discharge plateaus are 0.60 V (consistent with DFT calculations[29]) and 0.38 V, respectively. Diffusion coefficients were calculated using the equations and parameters shown in Text S1 (Supporting Information). The Al-ion diffusion coefficients for the first (0.60 V) and second (0.38 V) discharge plateaus were on the order of 10^{-19} cm^2/s and 10^{-16} cm^2/s, respectively. Solid-state Al^{3+} diffusion is thus three orders-of-magnitude slower during the first discharge plateau, consistent with the variable-temperature galvanostatic cycling data. Similarly, variable-rate galvanostatic cycling at 50 °C (Figure 1d) shows that greater current densities decrease the capacity of the first discharge plateau more rapidly, compared to the second one, while the overall capacity decreases and overpotential increases because of diffusion limitations. When the current density was decreased from 10 to 2 mA/g at 25 °C, the capacity and potential of the first discharge plateau increased, while the full capacity was recovered (Figure S4). A GITT measurement performed during the first discharge reveals large increases in irreversible capacity and overpotential associated with initial electrolyte decomposition (Figure S5).[14,19]

The chevrel crystal structure was preserved upon cycling, and its cubic morphology remained intact, as shown by XRD and SEM measurements (Figure S6 and Text S2), consistent with reversible aluminum-ion intercalation. If the electrochemical reaction were instead a conversion process that involved breaking and forming chemical bonds, the active material would dissolve and recrystallize, resulting in a change of morphology of the electrode particles.[30] Note that the chloroaluminate-containing $AlCl_3$:[EMIm]Cl ionic liquid electrolytes are corrosive and have been shown to react with other proposed electrode materials, such as V_2O_5,[31,32] as shown by Wen et al.[33]

To understand the electrochemical aluminum-ion intercalation mechanism into chevrel phase Mo_6S_8 at the molecular level, solid-state ^{27}Al single-pulse MAS NMR measurements were performed on cycled electrodes at different states-of-charge over two galvanostatic discharge−charge cycles (Figure 2). The NMR experiments were performed under quantitative conditions by using (i) short radiofrequency (rf) pulses ($\pi/12$) within the linear excitation regime for quadrupolar ^{27}Al nuclei (spin-5/2)[34,35] and (ii) recycle delays (0.1 s) such that the ^{27}Al nuclear spins relaxed to thermal equilibrium between measurements (Methods, Supporting Information). The cycled electrodes were rinsed with anhydrous methanol to remove electrolyte and surface species (see below), revealing two ^{27}Al signals at 62 and 38 ppm associated with aluminum ions intercalated within cavities 1 and 2, respectively. Their absolute and relative populations change during cycling as Al^{3+} ions intercalate and deintercalate within the Mo_6S_8 structure, establishing Al^{3+} intercalation. Their ^{27}Al shifts are consistent with tetrahedrally coordinated aluminum environments, as predicted by DFT calculations,[36] further confirming Al^{3+} intercalation.

The ^{27}Al NMR signals centered at 3 ppm are attributed to insoluble surface species whose ^{27}Al shifts are consistent with octahedrally coordinated environments. These species appear even before appreciable intercalation of aluminum ions occurs (Figure 2, spectrum at 1.4 V). Their absolute ^{27}Al signal intensity, scaled by sample mass, are approximately independent of state-of-charge (within ∼15%) after the first discharge is complete. Rinsing the electrode with different solvents other than anhydrous methanol (e.g., dichloromethane, acetonitrile, dimethylformamide, and chloroform) did not remove ^{27}Al signals in this region (Figure S7). Thus, the surface species are attributed to insoluble electrolyte decomposition products that form during the first discharge. While the precise nature of these ^{27}Al signals remains a topic of investigation, the results establish that they are associated with insoluble octahedrally coordinated aluminum surface species.

To quantify the amount of intercalated aluminum ions during galvanostatic cycling, the solid-state ^{27}Al single-pulse MAS NMR spectra were deconvoluted and their populations were tracked as a function of state-of-charge (Methods, Supporting Information). For example, deconvoluted ^{27}Al NMR spectra are shown for electrodes cycled to three different states-of-charge during the initial charge (Figure 3). The relative populations of aluminum ions in each cavity, obtained by their relative integrated ^{27}Al signal intensities, are thus revealed throughout the intercalation process (Table 1). In

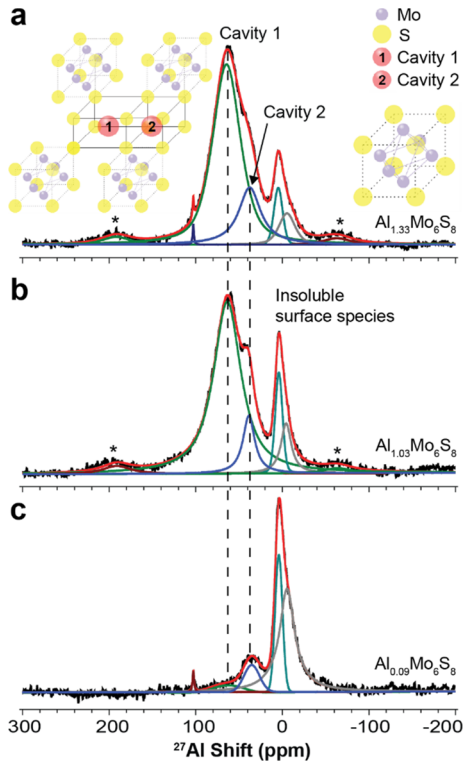

Figure 3. Quantitative deconvolutions of solid-state ^{27}Al single-pulse MAS NMR spectra acquired during first charge (deintercalation). (a) Discharged to 0.1 V, (b) charged to 0.5 V, and (c) charged to 1.2 V. Asterisks denote spinning side bands.

https://dx.doi.org/10.1021/acsenergylett.0c01138
ACS Energy Lett. 2020, 5, 2842−2848

Table 1. Intercalated Al^{3+} Cation Populations and Electrode Compositions Obtained from Quantitative Solid-State ^{27}Al Single-Pulse MAS NMR Measurements

	Al^{3+} populations (%)			
state-of-charge	cavity 1 (62 ppm)	cavity 2 (38 ppm)	x in $Al_xMo_6S_8$ (theoretical formula)	x in $Al_xMo_6S_8$ (from NMR)
1.4 V	81	19	0	0.03
0.5 V	71	29	0	0.16
0.4 V	90	10	1	1.06
0.1 V	78	22	1.33	1.33
0.5 V	88	12	1	1.03
1.2 V	24	76	0	0.09
0.1 V	82	18	1.33	1.12
0.5 V	82	18	1	1.02
1.2 V	35	65	0	0.09

addition, the absolute ^{27}Al signal intensity associated with intercalated aluminum ions, scaled by sample mass, was used to quantify the $Al_xMo_6S_8$ electrode compositions, where ^{27}Al signal intensity in the fully intercalated electrode was calibrated to $Al_{4/3}Mo_6S_8$. The solid-state NMR results are in excellent agreement with the expected theoretical compositions (Table 1). This result establishes that absolute NMR signal intensity can be used as an estimate of the overall extent of ion intercalation within cycled battery electrodes. An electrode sample with a known composition and mass can thus be used as an external standard for solid-state NMR spin-counting experiments. Care must be taken to ensure consistent tuning and matching between samples.

The quantitative solid-state ^{27}Al NMR measurements reveal several insights into the Al-ion intercalation mechanism. First, the aluminum ions intercalate into both cavities simultaneously, as opposed to sequentially (e.g., cavity 1 during the first discharge plateau and then cavity 2 during the second discharge plateau, as initially proposed by Lee et al.[14]). This phenomenon is revealed experimentally by direct spectroscopic characterization of the aluminum ions themselves. This result (i) agrees with Geng et al.,[19] who suggest simultaneous Al^{3+} intercalation by crystallographic analysis, and (ii) corroborates our interpretation of the additional reduction peak in the CV scans (Figure 1b). Al^{3+} intercalation thus differs notably from Mg^{2+} intercalation into chevrel Mo_6S_8,[25] where two distinct discharge plateaus correspond to sequential intercalation into cavity 1 and 2, likely because of stronger cation−cation repulsions among the more highly charged Al^{3+} cations.

Second, after charge (deintercalation), the solid-state ^{27}Al NMR results establish that only small quantities of trapped aluminum ions remain in the cavities ($Al_{0.09}Mo_6S_8$, or <7% of total intercalated Al^{3+} ions), the majority of which remain within cavity 2. This result differs from Mg^{2+} intercalation into chevrel Mo_6S_8, where significantly greater ion trapping occurs because of the higher activation energy barrier for Mg^{2+} ion hopping between the two cavities (0.57 eV, predicted via DFT[16]) compared to that for Al^{3+} (0.25 eV[26]). Thus, solid-state ^{27}Al NMR spectra reveal experimentally lesser extents of Al^{3+} ion-trapping compared to Mg^{2+}, consistent with DFT calculations of ion diffusion barriers. The Al-ion intercalation process is highly reversible, as demonstrated by solid-state ^{27}Al single-pulse MAS NMR measurements acquired after multiple cycles (Figure S8, 10th discharge). Similarly, solid-state ^{27}Al NMR spectra of electrodes discharged at 25 and 50 °C show no differences (Figure S9), as expected.

The intercalated Al^{3+} cations rapidly hop among six energetically equivalent sites within each cavity,[26] resulting in stochastic reorientations of the local ^{27}Al electric field gradient (EFG) that induce fast quadrupolar NMR relaxation. Notably, the solid-state ^{27}Al free-induction decays (FIDs) dissipated in less than 300 μs. The ^{27}Al signals could not be inverted (see ^{27}Al nutation curve, Figure S10). Attempts to measure ^{27}Al longitudinal T_1 NMR relaxation times were not successful: inversion recovery experiments were not possible, while signal saturation could not be achieved for saturation recovery experiments. Nevertheless, the fast decay of the signal FIDs is a manifestation of fast electric quadrupolar relaxation in the time domain, consistent with rapid atomic motions within the chevrel cavities. Acquisition of 2D $^{27}Al\{^{27}Al\}$ NMR correlation experiments[37] was not possible because of the short ^{27}Al spin coherence times, though it may be possible for other Al-ion intercalation electrodes.

Interestingly, when solid-state ^{27}Al single-pulse MAS NMR measurements were performed on a fully discharged "untreated" electrode that was not rinsed with anhydrous methanol, additional ^{27}Al NMR signals were observed (Figure 4). This result suggests that a surface layer forms during the first discharge, which is removed upon rinsing with solvent to reveal the ^{27}Al signals at 62 and 38 ppm associated with intercalated aluminum ions within cavity 1 and cavity 2, respectively, as well as the insoluble surface species discussed above. A 2D $^{27}Al\{^{27}Al\}$ exchange spectroscopy (EXSY) NMR experiment performed on the "untreated" electrode shows that the ^{27}Al signal at 84.4 ppm exchanges with the chloroaluminate ^{27}Al signals at 103.2 and 97.2 ppm associated with $AlCl_4^-$ and $Al_2Cl_7^-$, respectively (Figure S11), and thus is associated with an aluminum-containing species in the electrolyte. The other ^{27}Al signals appear to be associated with solid aluminum-containing moieties in a range of tetrahedral and octahedral environments. The surface layer was not observed in XRD (Figure S6), indicating that it is amorphous.

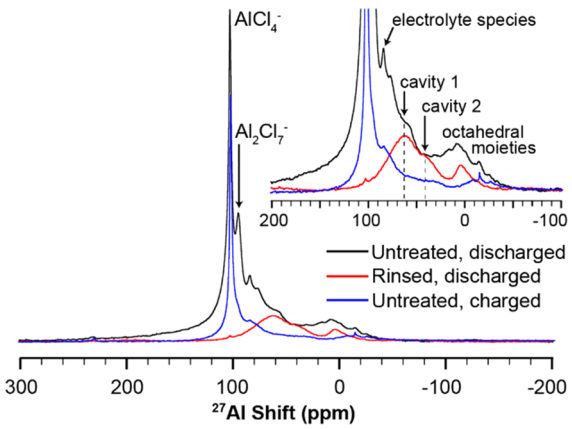

Figure 4. Solid-state ^{27}Al single-pulse MAS NMR spectra acquired on untreated discharged (0.1 V, $Al_{4/3}Mo_6S_8$, black) and charged (1.4 V, Mo_6S_8, blue) chevrel electrodes, as well as a discharged electrode rinsed with anhydrous methanol ($Al_{4/3}Mo_6S_8$, red).

We hypothesize that a surface layer forms reversibly because of the desolvation of Al^{3+} cations from chloroaluminate anions, a process that is not well understood at a molecular level. Desolvation would generate four Cl^- anions per Al^{3+} cation at

https://dx.doi.org/10.1021/acsenergylett.0c01138
ACS Energy Lett. 2020, 5, 2842−2848

the electrode−electrolyte interface, where the build-up of negative charge would be expected to be unstable. In Mg-ion batteries with chevrel Mo_6S_8 electrodes using organochloroaluminate/tetrahydrofuran electrolytes, DFT calculations predict that Mg^{2+} cation intercalation is faciliated by adsorption of intermediate $Mg_xCl_y^+$ species on the chevrel surface.[38] In this system, an analagous process may play an important role in Al^{3+} intercalation. Further investigation is required to understand the origin and composition of this amorphous surface layer. Note that the insoluble octahedrally coordinated aluminum surface species that form because of irreversible electrolyte decomposition during the first galvanostatic discharge are distinct and result from a different process.

In summary, the reversible electrochemical intercalation of aluminum cations into a model crystalline battery electrode, the chevrel Mo_6S_8, was quantitatively analyzed for the first time up from the molecular level. Electrochemical, XRD, SEM, and solid-state NMR measurements establish highly reversible Al-ion intercalation into chevrel Mo_6S_8. Solid-state ^{27}Al single-pulse MAS NMR measurements conducted under quantitative conditions establish that aluminum ions intercalate simultaneously, as opposed to sequentially, into two distinct cavities during galvanostatic discharge. Simultaneous intercalation was corroborated electrochemically by the appearance of an additional reduction peak in the cyclic voltammograms. Upon deintercalation, minimal quantities of trapped Al^{3+} ions remain (<7%). The slow solid-state ion diffusion measured electrochemically and the simultaneous ion intercalation mechanism can both be understood in terms of the high charge density of trivalent Al^{3+} cations: strong electrostatic attractions between Al^{3+} cations and the anionic chalcogen framework result in high activation energies for solid-state diffusion, while upon increasing extents of ion intercalation, strong electrostatic repulsions between molecularly proximate Al^{3+} ions force them to "hop" between cavities. Al-ion intercalation differs notably from Mg-ion intercalation into chevrel Mo_6S_8, wherein Mg^{2+} ions intercalate sequentially into each cavity during subsequent galvanostatic discharge plateaus and remain trapped in higher quantities upon deintercalation. Lastly, solid-state ^{27}Al MAS NMR measurements revealed that an amorphous layer forms on the surface of the chevrel electrode, whose formation appears to be reversible and linked to the desolvation of Al^{3+} cations from molecular chloroaluminate anions in the ionic liquid electrolyte. Overall, these results reveal quantitative molecular-level insights into the aluminum-ion intercalation mechanism in a model crystalline electrode and establish solid-state ^{27}Al MAS NMR spectroscopy as a powerful analytical technique to study rechargeable aluminum-ion batteries.

■ ASSOCIATED CONTENT

Supporting Information

The Supporting Information is available free of charge at https://pubs.acs.org/doi/10.1021/acsenergylett.0c01138.

Experimental methods, additional cyclic voltammetry and galvanostatic cycling data, differential capacity plots, GITT calculations of Al-ion diffusion coefficients, XRD and SEM measurements of cycled electrodes, and additional solid-state ^{27}Al NMR measurements (PDF)

■ AUTHOR INFORMATION

Corresponding Author

Robert J. Messinger − *Department of Chemical Engineering, The City College of New York, CUNY, New York, New York 10031, United States;* orcid.org/0000-0002-5537-3870; Email: rmessinger@ccny.cuny.edu

Authors

Ankur L. Jadhav − *Department of Chemical Engineering, The City College of New York, CUNY, New York, New York 10031, United States;* orcid.org/0000-0002-6481-4084

Jeffrey H. Xu − *Department of Chemical Engineering, The City College of New York, CUNY, New York, New York 10031, United States;* orcid.org/0000-0003-3404-4194

Complete contact information is available at: https://pubs.acs.org/10.1021/acsenergylett.0c01138

Notes

The authors declare no competing financial interest.

■ ACKNOWLEDGMENTS

The authors gratefully acknowledge the U.S. National Science Foundation (NSF CAREER award no. 1847552) and the U.S. Nuclear Regulatory Commission (NRC award no. 31310018M0036) for their support. NMR measurements were acquired in the City University of New York (CUNY) Advanced Science Research Center (ASRC) NMR facility.

■ REFERENCES

(1) Elia, G. A.; Marquardt, K.; Hoeppner, K.; Fantini, S.; Lin, R.; Knipping, E.; Peters, W.; Drillet, J. F.; Passerini, S.; Hahn, R. An Overview and Future Perspectives of Aluminum Batteries. *Adv. Mater.* **2016**, *28* (35), 7564−7579.

(2) Zafar, Z. A.; Imtiaz, S.; Razaq, R.; Ji, S.; Huang, T.; Zhang, Z.; Huang, Y.; Anderson, J. A. Cathode Materials for Rechargeable Aluminum Batteries: Current Status and Progress. *J. Mater. Chem. A* **2017**, *5* (12), 5646−5660.

(3) Muldoon, J.; Bucur, C. B.; Gregory, T. Quest for Nonaqueous Multivalent Secondary Batteries: Magnesium and Beyond. *Chem. Rev.* **2014**, *114* (23), 11683−11720.

(4) Lin, M.-C.; Gong, M.; Lu, B.; Wu, Y.; Wang, D.-Y.; Guan, M.; Angell, M.; Chen, C.; Yang, J.; Hwang, B.-J.; Dai, H. An Ultrafast Rechargeable Aluminium-Ion Battery. *Nature* **2015**, *520* (7547), 324−328.

(5) Huynh, T. C.; Dao, Q. P. D.; Truong, T.-N.; Doan, N.-G.; Ho, S.-L. Electrodeposition of Aluminum on Cathodes in Ionic Liquid Based Choline Chloride/Urea/$AlCl_3$. *Environ. Pollut.* **2014**, *3* (4), 59−69.

(6) Chu, W.; Zhang, X.; Wang, J.; Zhao, S.; Liu, S.; Yu, H. A Low-Cost Deep Eutectic Solvent Electrolyte for Rechargeable Aluminum-Sulfur Battery. *Energy Storage Mater.* **2019**, *22*, 418−423.

(7) Wu, Y.; Gong, M.; Lin, M. C.; Yuan, C.; Angell, M.; Huang, L.; Wang, D. Y.; Zhang, X.; Yang, J.; Hwang, B. J.; Dai, H. 3D Graphitic Foams Derived from Chloroaluminate Anion Intercalation for Ultrafast Aluminum-Ion Battery. *Adv. Mater.* **2016**, *28* (41), 9218−9222.

(8) Xu, J. H.; Turney, D. E.; Jadhav, A. L.; Messinger, R. J. Effects of Graphite Structure and Ion Transport on the Electrochemical Properties of Rechargeable Aluminum−Graphite Batteries. *ACS Appl. Energy Mater.* **2019**, *2* (11), 7799−7810.

(9) Saha, P.; Jampani, P. H.; Datta, M. K.; Hong, D.; Okoli, C. U.; Manivannan, A.; Kumta, P. N. Electrochemical Performance of Chemically and Solid State-Derived Chevrel Phase Mo_6T_8 (T = S, Se) Positive Electrodes for Sodium-Ion Batteries. *J. Phys. Chem. C* **2015**, *119* (11), 5771−5782.

(10) Aselmann, G.; Müller-Warmuth, W. ^{7}Li NMR Studies in Chevrel Phases $Li_XMo_6X_8$. *Z. Phys. Chem.* **1987**, *151*, 103−111.
(11) Aurbach, D.; Lu, Z.; Schechter, A.; Gofer, Y.; Gizbar, H.; Turgeman, R.; Cohen, Y.; Moshkovich, M.; Levi, E. Prototype Systems for Rechargeable Magnesium Batteries. *Nature* **2000**, *407* (6805), 724−727.
(12) Cheng, Y.; Luo, L.; Zhong, L.; Chen, J.; Li, B.; Wang, W.; Mao, S. X.; Wang, C.; Sprenkle, V. L.; Li, G.; Liu, J. Highly Reversible Zinc-Ion Intercalation into Chevrel Phase Mo_6S_8 Nanocubes and Applications for Advanced Zinc-Ion Batteries. *ACS Appl. Mater. Interfaces* **2016**, *8* (22), 13673−13677.
(13) Geng, L.; Lv, G.; Xing, X.; Guo, J. Reversible Electrochemical Intercalation of Aluminum in Mo_6S_8. *Chem. Mater.* **2015**, *27* (14), 4926−4929.
(14) Lee, B.; Lee, H. R.; Yim, T.; Kim, J. H.; Lee, J. G.; Chung, K. Y.; Cho, B. W.; Oh, S. H. Investigation on the Structural Evolutions during the Insertion of Aluminum Ions into Mo_6S_8 Chevrel Phase. *J. Electrochem. Soc.* **2016**, *163* (6), A1070−A1076.
(15) Levi, E.; Gershinsky, G.; Aurbach, D.; Isnard, O.; Ceder, G. New Insight on the Unusually High Ionic Mobility in Chevrel Phases. *Chem. Mater.* **2009**, *21* (7), 1390−1399.
(16) Ling, C.; Suto, K. Thermodynamic Origin of Irreversible Magnesium Trapping in Chevrel Phase Mo_6S_8: Importance of Magnesium and Vacancy Ordering. *Chem. Mater.* **2017**, *29* (8), 3731−3739.
(17) Levi, E.; Aurbach, D. Chevrel Phases, $M_xMo_6T_8$ (M = Metals, T = S, Se, Te) as a Structural Chameleon: Changes in the Rhombohedral Framework and Triclinic Distortion. *Chem. Mater.* **2010**, *22* (12), 3678−3692.
(18) Levi, E.; Lancry, E.; Mitelman, A.; Aurbach, D.; Isnard, O.; Djurado, D. Phase Diagram of Mg Insertion into Chevrel Phases, $Mg_xMo_6T_8$ (T = S, Se). 2. THe Crystal Structure of Triclinic $MgMo_6Se_8$. *Chem. Mater.* **2006**, *18* (16), 3705−3714.
(19) Geng, L.; Scheifers, J. P.; Zhang, J.; Bozhilov, K. N.; Fokwa, B. P. T.; Guo, J. Crystal Structure Transformation in Chevrel Phase Mo_6S_8 Induced by Aluminum Intercalation. *Chem. Mater.* **2018**, *30* (23), 8420−8425.
(20) Liu, H.; Choe, M. J.; Enrique, R. A.; Orvañanos, B.; Zhou, L.; Liu, T.; Thornton, K.; Grey, C. P. Effects of Antisite Defects on Li Diffusion in $LiFePO_4$ Revealed by Li Isotope Exchange. *J. Phys. Chem. C* **2017**, *121* (22), 12025−12036.
(21) Messinger, R. J.; Ménétrier, M.; Salager, E.; Boulineau, A.; Duttine, M.; Carlier, D.; Ateba Mba, J. M.; Croguennec, L.; Masquelier, C.; Massiot, D.; Deschamps, M. Revealing Defects in Crystalline Lithium-Ion Battery Electrodes by Solid-State NMR: Applications to $LiVPO_4F$. *Chem. Mater.* **2015**, *27* (15), 5212−5221.
(22) Pecher, O.; Carretero-Gonzalez, J.; Griffith, K. J.; Grey, C. P. Materials' Methods: NMR in Battery Research. *Chem. Mater.* **2017**, *29* (1), 213−242.
(23) Xu, J. H.; Jadhav, A. L.; Turney, D. E.; Messinger, R. J. Molecular-Level Environments of Intercalated Chloroaluminate Anions in Rechargeable Aluminum- Graphite Batteries Revealed by Solid-State NMR Spectroscopy. *J. Mater. Chem. A* **2020**, DOI: 10.1039/D0TA02611E.
(24) Grey, C. P.; Dupré, N. NMR Studies of Cathode Materials for Lithium-Ion Rechargeable Batteries. *Chem. Rev.* **2004**, *104* (10), 4493−4512.
(25) Levi, E.; Lancry, E.; Mitelman, A.; Aurbach, D.; Ceder, G.; Morgan, D.; Isnard, O. Phase Diagram of Mg Insertion into Chevrel Phases, $Mg_XMo_6T_8$ (T = S, Se). 1. Crystal Structure of the Sulfides. *Chem. Mater.* **2006**, *18* (23), 5492−5503.
(26) Agiorgousis, M. L.; Sun, Y.-Y.; West, D. J.; Zhang, S. Intercalated Chevrel Phase Mo_6S_8 as a Janus Material for Energy Generation and Storage. *ACS Appl. Energy Mater.* **2018**, *1*, 440.
(27) Zhu, Y.; Gao, T.; Fan, X.; Han, F.; Wang, C. Electrochemical Techniques for Intercalation Electrode Materials in Rechargeable Batteries. *Acc. Chem. Res.* **2017**, *50* (4), 1022−1031.
(28) Wen, C. J. Thermodynamic and Mass Transport Properties of "LiAl. *J. Electrochem. Soc.* **1979**, *126* (12), 2258.
(29) Juran, T. R.; Smeu, M. Hybrid Density Functional Theory Modeling of Ca, Zn, and Al Ion Batteries Using the Chevrel Phase Mo_6S_8 Cathode. *Phys. Chem. Chem. Phys.* **2017**, *19* (31), 20684−20690.
(30) Canepa, P.; Sai Gautam, G.; Hannah, D. C.; Malik, R.; Liu, M.; Gallagher, K. G.; Persson, K. A.; Ceder, G. Odyssey of Multivalent Cathode Materials: Open Questions and Future Challenges. *Chem. Rev.* **2017**, *117* (5), 4287−4341.
(31) Gu, S.; Wang, H.; Wu, C.; Bai, Y.; Li, H.; Wu, F. Confirming Reversible Al^{3+} Storage Mechanism through Intercalation of Al^{3+} into V_2O_5 Nanowires in a Rechargeable Aluminum Battery. *Energy Storage Mater.* **2017**, *6*, 9−17.
(32) Wang, H.; Bai, Y.; Chen, S.; Luo, X.; Wu, C.; Wu, F.; Lu, J.; Amine, K. Binder-Free V_2O_5 Cathode for Greener Rechargeable Aluminum Battery. *ACS Appl. Mater. Interfaces* **2015**, *7* (1), 80−84.
(33) Wen, X.; Liu, Y.; Jadhav, A.; Zhang, J.; Borchardt, D.; Shi, J.; Wong, B. M.; Sanyal, B.; Messinger, R. J.; Guo, J. Materials Compatibility in Rechargeable Aluminum Batteries: Chemical and Electrochemical Properties between Vanadium Pentoxide and Chloroaluminate Ionic Liquids. *Chem. Mater.* **2019**, *31* (18), 7238−7247.
(34) Fenzke, D.; Freude, D.; Fröhlich, T.; Haase, J. NMR Intensity Measurements of Half-Integer Quadrupole Nuclei. *Chem. Phys. Lett.* **1984**, *111* (1−2), 171−175.
(35) Samoson, A.; Lippmaa, E. Excitation Phenomena and Line Intensities in High-Resolution NMR Powder Spectra of Half-Integer Quadrupolar Nuclei. *Phys. Rev. B: Condens. Matter Mater. Phys.* **1983**, *28* (11), 6567.
(36) Charpentier, T.; Menziani, M. C.; Pedone, A. Computational Simulations of Solid State NMR Spectra: A New Era in Structure Determination of Oxide Glasses. *RSC Adv.* **2013**, *3* (27), 10550−10578.
(37) Haouas, M.; Taulelle, F.; Martineau, C. Recent Advances in Application of ^{27}Al NMR Spectroscopy to Materials Science. *Prog. Nucl. Magn. Reson. Spectrosc.* **2016**, *94*−*95*, 11−36.
(38) Wan, L. F.; Perdue, B. R.; Apblett, C. A.; Prendergast, D. Mg Desolvation and Intercalation Mechanism at the Mo_6S_8 Chevrel Phase Surface. *Chem. Mater.* **2015**, *27* (17), 5932−5940.

https://dx.doi.org/10.1021/acsenergylett.0c01138
ACS Energy Lett. 2020, 5, 2842−2848